Dynamic conductivity scaling in photoexcited V_2O_3 thin films

Elsa Abreu,[1,*] Siming Wang,[2,3,4] Juan Gabriel Ramírez,[2,3] Mengkun Liu,[2,5] Jingdi Zhang,[1,2] Kun Geng,[1] Ivan K. Schuller,[2,3,4] and Richard D. Averitt[1,2,†]

[1]*Department of Physics, Boston University, Boston, Massachusetts 02215, USA*
[2]*Department of Physics, The University of California at San Diego, La Jolla, California 92093, USA*
[3]*Center for Advanced Nanoscience, The University of California at San Diego, La Jolla, California 92093, USA*
[4]*Materials Science and Engineering Program, The University of California at San Diego, La Jolla, California 92093, USA*
[5]*Department of Physics, Stony Brook University, Stony Brook, New York 11794, USA*

Optical-pump terahertz-probe spectroscopy is used to investigate ultrafast far-infrared conductivity dynamics during the insulator-to-metal transition in vanadium sesquioxide (V_2O_3). The resultant conductivity increase occurs on a tens of picosecond time scale, exhibiting a strong dependence on the initial temperature and fluence. We have identified a scaling of the conductivity dynamics upon renormalizing the time axis with a simple power law ($\alpha \simeq 1/2$) that depends solely on the initial, final, and conductivity onset temperatures. Qualitative and quantitative considerations indicate that the dynamics arise from nucleation and growth of the metallic phase which can be described by the Avrami model. We show that the temporal scaling arises from spatial scaling of the growth of the metallic volume fraction, highlighting the self-similar nature of the dynamics. Our results illustrate the important role played by mesoscopic effects in phase transition dynamics.

PACS number(s): 78.47.J−, 64.60.−i, 68.55.A−, 71.30.+h

I. INTRODUCTION

The variety of electronic, magnetic, and structural phases exhibited by transition-metal oxides arise from a delicate balance between competing degrees of freedom whose contribution to the macroscopic properties is challenging to ascertain [1]. An increasingly successful approach to this problem is that of time-resolved experiments, where ultrafast excitation and probing enables the determination of fundamental material time scales down to femtosecond resolution [2–4]. Access to specific energy scales is made possible by ultrafast sources ranging from terahertz (THz) to x-ray frequencies. Initial all-optical measurements of electron-phonon relaxation in metals [5,6] have paved the way to time-resolved investigations of complex systems, from spins in magnetic materials [7–11] to superconducting gaps [12,13] or to surface charges in topological insulators [14].

To date, most time-resolved experiments in transition-metal oxides, and in particular vanadates, have focused on microscopic dynamics [15–22]. For example, fast subpicosecond electronic and structural responses have been reported for vanadium dioxide [15–17,19,21,22]. However, static measurements increasingly demonstrate that nano-to-mesoscale phase coexistence is crucial in determining the properties of complex materials, including cuprates, manganites, and vanadates [23–27]. This naturally extends to dynamic investigations of the phase coexistence stage, as done in VO_2 [19,22,28,29]. At a minimum, neglecting mesoscale effects can lead to a misinterpretation of the dynamics. More importantly, as shown in this work, mesoscale dynamics are of intrinsic interest from fundamental and applied perspectives.

V_2O_3 is a paramagnetic metal with rhombohedral crystal symmetry [30–35] which undergoes a first order phase transition to an antiferromagnetic insulating state at $T_{IMT} = 175$ K, accompanied by a change to a monoclinic crystal structure [36]. In this work, we present mesoscopic conductivity dynamics of V_2O_3 across the insulator-to-metal transition following an optically initiated picosecond thermal quench into the metallic state. Importantly, we identify scaling of the conductivity dynamics upon renormalizing the time axis with a simple power law ($\alpha \simeq 1/2$), dependent solely on *experimentally determined temperatures*. These are the initial temperature T_i, final temperature T_f (determined by T_i and the incident fluence, F_{inc}), and conductivity onset temperature $T_{0.5} = 160$ K (marking the onset of a macroscopic THz conductivity which, in two dimensions (2D), occurs at a volume fraction of $f = 0.5$). Further, the temporal evolution of the conductivity is well fit by the Avrami model, consistent with nucleation and growth of the metallic phase. This enables us to conclude that the temporal rescaling arises from spatial scaling of the metallic volume fraction. Insulator-to-metal transition (IMT) conductivity dynamics are therefore dictated by a mesoscopic length scale, $R(t)$, associated with metallic phase domain coarsening. Our analysis further indicates that the metallic phase grows ballistically, at the sound velocity.

II. EXPERIMENTAL RESULTS AND ANALYSIS

95-nm-thick V_2O_3 films were grown in an ultrahigh purity Ar environment by rf magnetron sputtering of a V_2O_3 target onto an r-plane ($10\bar{1}2$) sapphire substrate [34]. X-ray diffraction characterization indicates near single crystal growth following the substrate orientation. Transient conductivity measurements are performed using 1.5 eV, 50 fs pulses from a 3 mJ Ti:sapphire amplifier. Incident pump fluences, 0.5–4 mJ/cm^2, remain below the V_2O_3 damage threshold [20]. THz pulses are nonlinearly generated in ZnTe, yielding a 0.1–2.5 THz bandwidth [37,38].

We first present the V_2O_3 static conductivity characterization from THz time-domain spectroscopy (i.e., the

———
*Present address: Institute for Quantum Electronics, Physics Department, ETH Zurich, 8093 Zurich, Switzerland;elsabreu@bu.edu
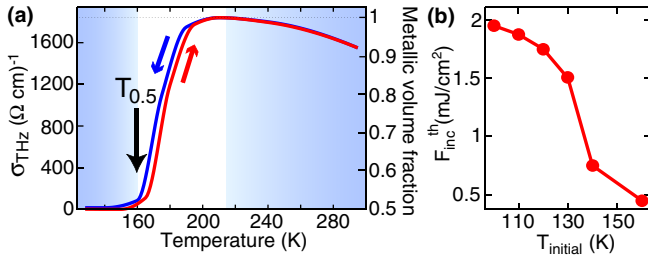†raveritt@ucsd.edu

FIG. 1. (Color online) (a) σ vs T from THz time-domain spectroscopy. The arrow marks the conductivity onset temperature, $T_{0.5} = 160$ K. $f(T)$, calculated from Eq. (1) for the unshaded region of the plot, is labeled on the right. (b) Fluence threshold for a finite $\Delta\sigma(t)$, with $T_i < T_{0.5}$.

photoexcitation is blocked). The temperature dependent real part of the Drude conductivity, $\sigma(T)$, is shown in Fig. 1(a). The IMT occurs at $T_{IMT} \simeq 175$ K, with a narrow hysteresis associated with its first order nature [39]. As indicated in Fig. 1(a), $T_{0.5} = 160$ K corresponds to the temperature above which a finite THz conductivity arises.

Optical-pump THz-probe experiments were performed for several T_i ($<T_{0.5}$) and F_{inc} values. Photoexcitation at 1.5 eV initiates an ultrafast heat quench in the film, and excited electrons relax via phonon emission in $\sim$1 ps (from the two temperature model [5,40–43]). In other words, heating of the system occurs in $\sim$1 ps, setting up a nonequilibrium situation where the insulating phase is unstable, which leads to metallic phase growth. Changes in the transient THz conductivity $\Delta\sigma(t)$ thus reflect nucleation and growth dynamics. One of the hallmarks of a photoinduced phase transition is the observation of a fluence threshold, F_{inc}^{th}, for the IMT onset, as shown in Fig. 1(b) as a function of T_i. F_{inc}^{th} decreases with increasing T_i, in line with what is observed in VO$_2$ [19,28]. F_{inc}^{th} is derived from detailed measurements of the conductivity

dynamics, which are considered in greater detail in Fig. 2. Figure 2(a) shows $\Delta\sigma(t)$ (for various T_i) for $F_{inc} = 3$ mJ/cm^2, corresponding to an absorbed energy density of $\sim$170 J/cm^3. $\sigma(t)$ increases over 10s of picoseconds following photoexcitation, and saturates at a value corresponding to $\sigma(T_f)$. In fact, comparison of $\sigma(t = 400$ ps, $T_f)$ with Fig. 1(a) provides a means to estimate T_f, consistent with two temperature model estimates (Fig. S2 [37]). Varying F_{inc} at fixed T_i leads to variations in T_f and consequently in $\Delta\sigma$, as shown in Fig. 2(b). Clearly, the dynamics depend on both T_i and T_f.

Further insight into the $\Delta\sigma(t)$ dynamics can be obtained by normalizing the data, as illustrated in Figs. 2(c) and 2(d). Figure 2(c) shows that the $\Delta\sigma(t)$ rise time is faster for increasing T_i. For instance, for $T_i = 80$ K the maximum in $\Delta\sigma(t)$ is reached in $\sim$120 ps, while for $T_i = 140$ K it takes $\sim$60 ps. The $\Delta\sigma(t)$ rise time is also faster for increasing F_{inc}, as shown in Fig. 2(d). A detailed analysis of these rise time dynamics is presented below and constitutes the main result of this work.

A partial recovery of $\Delta\sigma(t)$ is observable with decreasing T_i [cf. Figs. 2(a) and 2(c)]. Recovery on this time scale is unlikely due to heat escape from the sample which typically takes several nanoseconds [44–46], though our data does not unequivocally rule out cooling as the cause for the 100-ps-scale $\Delta\sigma(t)$ decrease. The recovery may be related to decreased stability of the metallic volume fraction distribution at low T_f, associated with a larger fraction of metallic regions whose characteristic dimensions are too small to undergo stable growth [47].

The qualitative discussion of conductivity dynamics presented above suggests the primary role of nucleation and growth, with a clear dependence on T_i and T_f. In the following, we investigate these dynamics in greater detail, first demonstrating their temperature dependent scaling. The temperature above which a macroscopic conductivity can be measured, $T_{0.5}$, is the critical temperature for the nucleation
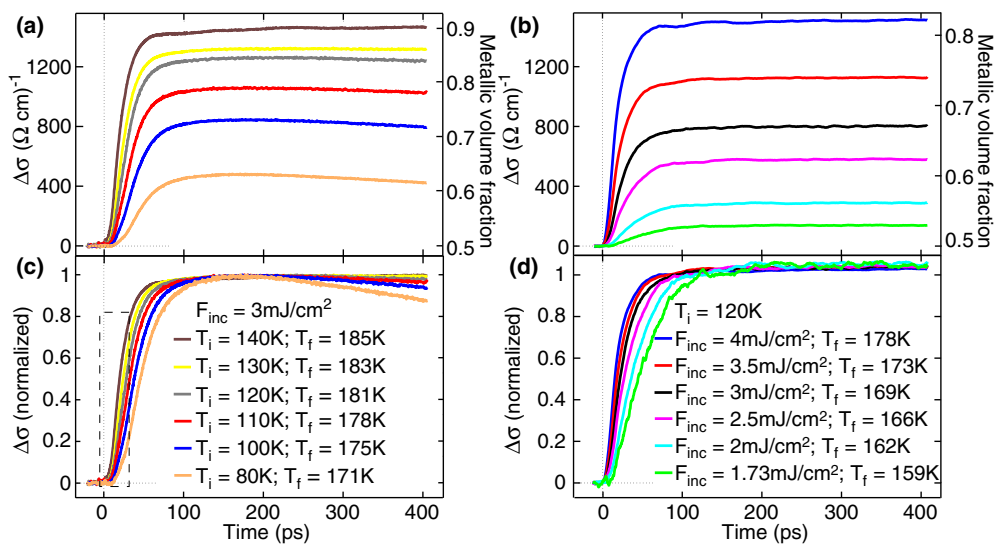

FIG. 2. (Color online) Conductivity dynamics of V$_2$O$_3$ films following (a) 3 mJ/cm^2 optical excitation, for $T_i < T_{0.5}$, and (b) 1.73–4 mJ/cm^2 optical excitation, for $T_i = 120$K. (c) and (d) Normalization of (a) and (b), respectively, revealing the T_i and F_{inc} dependence of the $\Delta\sigma(t)$ rise time. [Figure 4(b) magnifies the region within the dashed box of (c).] (a) and (c) were obtained from a different sample than (b) and (d), highlighting a slight sample-to-sample variation of the $\Delta\sigma(t)$ rise time.
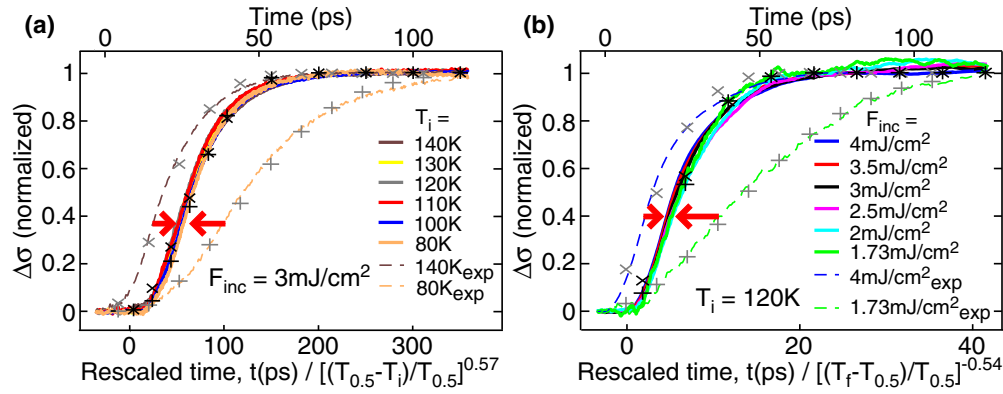
FIG. 3. (Color online) Normalized conductivity dynamics for (a) $F_{inc} = 3$ mJ/cm^2, with varying T_i, and for (b) $T_i = 120$ K, with varying F_{inc}. The bottom (top) time axis corresponds to the scaled (unscaled) data, shown by full (dashed) lines. Note that $t = 0$ for the top and bottom axes is offset for clarity. Gray (black) crosses correspond to fits (scaled fits) to the (a) 80 and 140 K data, and the (b) 1.73 and 4 mJ/cm^2 data, using Eq. (2) with $n = 2$.

and growth process that underlies the IMT. It is therefore reasonable to expect a dependence of IMT dynamic properties on $|T - T_{0.5}|$ [48]. As shown in Fig. 3, the $\Delta\sigma(t)$ curves collapse by scaling the time axis. In Fig. 3(a) F_{inc} is fixed at 3 mJ/cm^2 and T_i is varied between 80 and 140 K [cf. Figs. 2(a) and 2(c)]. Scaling of the time axis by a dimensionless factor, $t \rightarrow t/(\frac{T_{0.5}-T_i}{T_{0.5}})^\alpha$, with $\alpha \simeq 1/2$, leads to a collapse of all the curves with different T_i values [Fig. 3(a)]. The same scaling leads to the collapse of $\Delta\sigma(t)$ dynamics for $F_{inc} = 2$ mJ/cm^2 (Fig. S3 [37]), which is close to F_{inc}^{th} at low temperatures [Fig. 1(b)]. However, varying T_i corresponds to a variation not only of T_i but also of T_f. A variation of T_f alone can be achieved by fixing T_i and varying F_{inc}. Figure 3(b) shows results for fixed $T_i = 120$ K and for F_{inc} between 1.73 and 4 mJ/cm^2 [cf. Figs. 2(b) and 2(d)]. A collapse of the normalized $\Delta\sigma(t)$ curves arises if the time axis is rescaled by $t \rightarrow t/(\frac{T_f-T_{0.5}}{T_{0.5}})^{-\alpha}$ [Fig. 3(b)]. Notably, the scaling behavior relies on the experimentally determined T_i, T_f, and $T_{0.5}$ values. The only parameter varied to achieve the scaling in Fig. 3 is the exponent α.

To determine the value of α that provides the best scaling of the data a scaling error was calculated [37]. Optimal values of α are seen to lie close to 1/2, and are used to scale the data in Figs. 3(a) and 3(b). This temporal scaling is quite remarkable, indicating that the processes underlying the conductivity dynamics must also exhibit scaling. Further, the mean-field-like exponent of 1/2 suggests that fluctuations are not dominant, and that a simple model can provide additional insights [49,50]. In the following, we consider these results in terms of nucleation and growth of the metallic volume fraction, $f(t)$.

The IMT in V$_2$O$_3$ arises from nucleation and growth of metallic domains in an insulating background [51–53]. The metallic volume fraction, $f(T)$, can be calculated from $\sigma(T)$ using the Bruggeman effective medium approximation:

$$f \frac{\sigma_m - \sigma}{\sigma_m + (d-1)\sigma} + (1-f)\frac{\sigma_i - \sigma}{\sigma_i + (d-1)\sigma} = 0, \quad (1)$$

where σ_m and σ_i correspond to metallic and insulating state conductivities, respectively, and the dimensionality $d = 2$ for thin films [28,54]. In the temperature range where $\sigma(T) \gg \sigma_i$,

taking $\sigma_i = 0$ is a valid approximation, and Eq. (1) yields a linear dependence of $\sigma(t)$ on $f(t)$, $\sigma(t) = [2f(t) - 1]\sigma_m$. The right axis of Fig. 1(a) shows $f(T)$ across the IMT. The correspondence between $\sigma(T)$ and $f(T)$ values derived from THz time-domain spectroscopy is strictly valid only in the ~160–200 K range [unshaded region of the $\sigma(T)$ curve]. For $T > 200$ K, $f(T) = 1$ and the decrease in $\sigma(T)$, consistent with previous reports, arises from correlation effects, beyond a simple thermally induced increase in the scattering rate [20,33–35]. For $T < 160$ K, the $\sigma_i = 0$ approximation in Eq. (1) breaks down. dc resistivity measurements yield a thermally activated $\sigma_i(T)$, which we use to estimate $f(T)$ below $T_{0.5} = 160$ K from Eq. (1). It is clear that a nonzero $\sigma_i(T)$ for $T < T_{0.5}$ implies a nonzero $f(T)$ well below $T_{0.5}$. This is an important consideration for time-resolved experiments, where the initial condition is a mixed phase with metallic volume fraction $f(T_i)$.

III. DISCUSSION

Classical models of nucleation and growth predict a dynamic evolution of the volume fraction $f(t)$, which can be described by the Avrami equation [55],

$$f(t) = 1 - e^{-Kt^n}, \quad (2)$$

where K is the rate at which $f(t)$ increases, and n is an exponent that depends on the dimensionality and nature of the nucleation and growth. As mentioned above, for $\sigma \gg \sigma_i$, a linear relationship exists between $\sigma(t)$ and $f(t)$. The photoinduced conductivity variations we measure, $\Delta\sigma(t)$, are therefore proportional to $f(t)$, and Eq. (2) can be used to fit the normalized $\Delta\sigma(t)$ data. A good fit is obtained for $n = 2$ [37], as illustrated by the gray crosses in Figs. 3(a) and 3(b). Rescaling the time axis effectively corresponds to a rescaling of K. This is highlighted by the rescaled fitting curves, shown as black crosses in Figs. 3(a) and 3(b), which are obtained by replacing K by $K/(\frac{T_{0.5}-T_i}{T_{0.5}})^{n\alpha}$ [Fig. 3(a)] and by $K/(\frac{T_f-T_{0.5}}{T_{0.5}})^{-n\alpha}$ [Fig. 3(b)] in Eq. (2), while keeping the time axis unchanged. Such a behavior implies a temperature dependence of K, $K \propto 1/(T_{0.5} - T_i)$ and $K \propto (T_f - T_{0.5})$, i.e., the IMT is faster for increasing T_i and T_f.
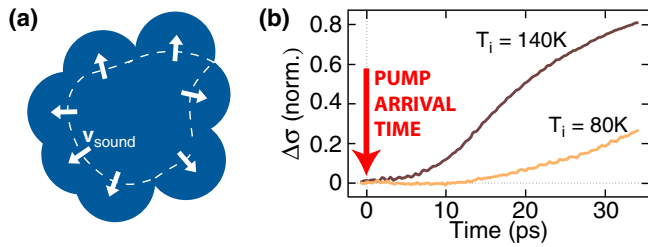
(a)

(b)

FIG. 4. (Color online) (a) Schematics of 2D nucleation and growth: growing (following photoexcitation) metallic regions are in blue; the white arrows indicate the radial growth velocity, $\sim v_{sound}$. (b) Delayed onset of $\Delta\sigma(t)$ for lower T_i, detailed from Fig. 2(c). No finite $\Delta\sigma(t)$ is visible during the first few picoseconds after the optical pump.

Both nucleation and growth contribute to K. In the current experiments, prior to the optically induced temperature quench, the sample is at T_i with a volume fraction of metallic nuclei $f_i = f(T_i)$. The ultrafast quench modifies the free energy landscape by shifting the minimum from the insulating to the metallic phase, characterized by T_f. Therefore, the energy gain associated with the IMT following photoexcitation drives the growth of metallic domains leading to an increasing volume fraction. A model that is consistent with $n = 2$ describes two-dimensional interfacial growth with quasi-instantaneous nucleation [37,55]. This yields

$$K = \pi\rho v^2, \qquad (3)$$

where ρ is the domain density and v is the growth velocity. A schematic of this process (in 2D) is shown in Fig. 4(a), with the metallic regions, shown in blue, growing at velocity v, as indicated by the white arrows. Equation (3) contains independent contributions from growth, through v, and nucleation, through ρ, allowing for additional insight into the experimental conductivity dynamics. We note that in thin film samples excited homogeneously across the entire thickness (the penetration depth of the optical pump is on the order of the film thickness) the growth is essentially 2D (in-plane growth) [54].

We first consider the growth of the metallic regions, where the interface (domain wall) separating the metallic and insulating phases propagates at v, defining a characteristic size given by the local radius of curvature $R(t) = v \times t$. It is worth noting that the structural transition which accompanies the IMT in V_2O_3 implies that v cannot exceed the propagation velocity for structural distortions, i.e., the sound velocity, v_{sound}. Growth of the metallic phase at v_{sound} would be ballistic rather than diffusive, in line with previous descriptions of thermally driven IMT in vanadates as martensitic, i.e., diffusionless [56,57]. An estimate of K using v_{sound} for V_2O_3 strongly suggests that growth is indeed in the ballistic limit. Assuming that ρ is given by the effective nuclei density $\rho = 5 \times 10^{12}$ m^{-2} [57] and taking $v_{sound} = 5 \times 10^3$ m/s [58] yields $K = 3.9 \times 10^{-4}$ ps^{-2}, consistent with the 30–70 ps rise times we observe [corresponding to $K^{-1/2}$, from Eq. (2)]. Of course the assumption that ρ corresponds to the equilibrium defect density is rather crude, but nonetheless confirms the applicability of the Avrami model and suggests interfacial ballistic growth of the

metallic phase as the underlying dynamics of the macroscopic conductivity increase following photoexcitation.

Given that the sound velocity in V_2O_3 varies little with temperature [58], the temperature dependence (and hence the scaling) of K arises from the nucleation processes that give rise to ρ. That is, in the T_i and T_f range we are exploring in these experiments, the metallic domain density ρ must exhibit $\rho \propto 1/(T_{0.5} - T_i)$ and $\rho \propto (T_f - T_{0.5})$. Also, since the growth is ballistic (i.e., it proceeds at the maximum allowed velocity), it is changes in ρ that determine the conductivity rise time dynamics. This means that, for increasing T_i, the initial domain density available for growth increases. Additionally, with increasing T_f, ρ increases meaning that the photoinduced thermal quench increases the domain density available for subsequent growth. Thus, the evolution of ρ is fairly complicated and strongly dependent on the details of the nucleation process.

Nucleation has been reported to occur preferentially at defect sites on VO_2 and V_2O_3 [35]. Such defect pinning effects can influence the IMT dynamics, leading to two limiting situations. For samples with a large defect density the nucleation is entirely heterogeneous and expected to occur instantaneously, so that all nuclei are immediately available for growth [55,57]. In clean samples, on the other hand, nucleation is essentially homogeneous and new nuclei formed during a finite period after the quench constitute a sizable fraction of the overall nuclei density from which the growth proceeds [55,59]. Neither of these limits appear to be completely verified in our experiments.

Importantly, the time delay, Δt, for the onset of $\Delta\sigma(t)$ [when $f(t) = 0.5$] following photoexcitation is quite long, on the order of a few picoseconds [Figs. 2 and 4(b)]. Δt is longer for lower T_i, as detailed in Fig. 4(b), where for $T_i = 80$ K, $\Delta t > 10$ ps, while for $T_i = 140$ K, $\Delta t \sim 5$ ps. The longer Δt for lower T_i is consistent with a smaller $f(T_i)$. We have observed that Δt is sample dependent (cf. Fig. 2) hinting at the possibility of variations of the nucleation process with defect density, such that films with a lower extrinsic defect density have a larger homogeneous nucleation contribution. However, homogeneous nucleation models predict an exponential increase of the nucleation rate (not to be confused with K) with superheating, i.e., with $T_f - T_{0.5}$ [37,55,59], while in the heterogeneous limit the dependence on $T_f - T_{0.5}$ becomes a power law [37,57]. Thus, the experimentally observed power law scaling attests to a significant heterogeneous contribution to the nucleation. Our analysis indicates that the dynamics can, to a certain extent, be controlled by the defect density. The higher the defect density, the faster the mesoscopic conductivity will be established after photoexcitation. This comes at the expense of a reduced metallic state conductivity because of increased defect scattering.

More detail will be achievable once samples with controllable defect densities become available [60], since our data suggests that a change in the T_f dependence of K is to be expected as nucleation becomes more homogeneous (for lower defect density). A change in the initial time delay, Δt [Fig. 4(b)], would also be expected with variations in defect density. That is, with heterogeneous dominated nucleation, Δt would be shorter since growth could proceed immediately, whereas for increasingly homogeneous nucleation, Δt would

increase since nuclei would need to be formed prior to growth. There is some evidence of this in our studies of different samples (cf. Fig. 2). Details of the scaling exponent α should be accessible by Monte Carlo simulations. Further insight into α can also be gained from considering different system dimensionalities [37]. As discussed in Ref. [37], the geometry of domain growth is sensitive to the dimensionality of the system, and so is n in Eq. (2). The dynamic scaling we identified provides a simple yet robust means to analyze nucleation and growth dynamics during first order transitions. In general, from an experimental perspective, an interesting follow-up to the present work would be to analyze samples with different morphologies and a controlled defect density, and using time-resolved techniques that reveal the spatial distribution of the metallic domains at the mesoscale.

IV. CONCLUSIONS

In summary, our investigation of the IMT conductivity dynamics in V_2O_3 thin films reveals the temperature dependence of domain growth through dynamic scaling of the $\Delta\sigma(t)$ rise time. These results highlight the importance of the mesoscale in shaping the dynamic evolution of first order IMTs. The temperature dependence of the dynamics provides additional control over the properties of transition-metal oxides. Also, this dependence must be taken into account when investigating materials where phase coexistence plays a significant role in the IMT.

[1] J. M. Rondinelli and N. A. Spaldin, Adv. Mater. **23**, 3363 (2011).

[2] I. K. Schuller and K. E. Gray, Phys. Rev. Lett. **36**, 429 (1976).

[3] J. Orenstein, Phys. Today **65**, 44 (2012).

[4] J. Zhang and R. D. Averitt, Annu. Rev. Mater. Res. **44**, 19 (2014).

[5] S. D. Brorson, A. Kazeroonian, J. S. Moodera, D. W. Face, T. K. Cheng, E. P. Ippen, M. S. Dresselhaus, and G. Dresselhaus, Phys. Rev. Lett. **64**, 2172 (1990).

[6] C.-K. Sun, F. Vallée, L. H. Acioli, E. P. Ippen, and J. G. Fujimoto, Phys. Rev. B **50**, 15337 (1994).

[7] M. van Kampen, C. Jozsa, J. T. Kohlhepp, P. LeClair, L. Lagae, W. J. M. de Jonge, and B. Koopmans, Phys. Rev. Lett. **88**, 227201 (2002).

[8] X. Zhu, Z. Liu, V. Metlushko, P. Grütter, and M. R. Freeman, Phys. Rev. B **71**, 180408(R) (2005).

[9] T. Kampfrath, A. Sell, G. Klatt, A. Pashkin, S. Ma, T. Dekorsy, M. Wolf, M. Fiebig, A. Leitenstorfer, and R. Huber, Nat. Photonics **5**, 31 (2011).

[10] C. Vicario, C. Ruchert, F. Ardana-Lamas, P. M. Derlet, B. Tudu, J. Luning, and C. P. Hauri, Nat. Photonics **7**, 720 (2013).

[11] C. E. Graves, A. H. Reid, T. Wang, B. Wu, S. de Jong, K. Vahaplar, I. Radu, D. P. Bernstein, M. Messerschmidt, L. Müller, R. Coffee, M. Bionta, S. W. Epp, R. Hartmann, N. Kimmel, G. Hauser, A. Hartmann, P. Holl, H. Gorke, J. H. Mentink *et al.*, Nat. Mater. **12**, 293 (2013).

[12] J. Demsar, R. D. Averitt, A. J. Taylor, V. V. Kabanov, W. N. Kang, H. J. Kim, E. M. Choi, and S. I. Lee, Phys. Rev. Lett. **91**, 267002 (2003).

[13] R. Matsunaga and R. Shimano, Phys. Rev. Lett. **109**, 187002 (2012).

[14] Y. H. Wang, H. Steinberg, P. Jarillo-Herrero, and N. Gedik, Science **342**, 453 (2013).

[15] A. Cavalleri, C. Tóth, C. W. Siders, J. A. Squier, F. Ráksi, P. Forget, and J. C. Kieffer, Phys. Rev. Lett. **87**, 237401 (2001).

[16] A. Cavalleri, T. Dekorsy, H. H. W. Chong, J. C. Kieffer, and R. W. Schoenlein, Phys. Rev. B **70**, 161102(R) (2004).

[17] C. Kubler, H. Ehrke, R. Huber, R. Lopez, A. Halabica, R. F. Haglund, and A. Leitenstorfer, Phys. Rev. Lett. **99**, 116401 (2007).

[18] B. Mansart, D. Boschetto, S. Sauvage, A. Rousse, and M. Marsi, Europhys. Lett. **92**, 37007 (2010).

[19] A. Pashkin, C. Kübler, H. Ehrke, R. Lopez, A. Halabica, R. F. Haglund, Jr., R. Huber, and A. Leitenstorfer, Phys. Rev. B **83**, 195120 (2011).

[20] M. K. Liu, B. Pardo, J. Zhang, M. M. Qazilbash, S. J. Yun, Z. Fei, J.-H. Shin, H.-T. Kim, D. N. Basov, and R. D. Averitt, Phys. Rev. Lett. **107**, 066403 (2011).

[21] S. Wall, D. Wegkamp, L. Foglia, K. Appavoo, J. Nag, R. F. Haglund, J. Stähler, and M. Wolf, Nat. Commun. **3**, 721 (2012).

[22] T. L. Cocker, L. V. Titova, S. Fourmaux, G. Holloway, H.-C. Bandulet, D. Brassard, J.-C. Kieffer, M. A. El Khakani, and F. A. Hegmann, Phys. Rev. B **85**, 155120 (2012).

[23] E. Dagotto, Science **309**, 257 (2005).

[24] D. N. Basov, R. D. Averitt, D. van der Marel, M. Dressel, and K. Haule, Rev. Mod. Phys. **83**, 471 (2011).

[25] M. M. Qazilbash, A. Tripathi, A. A. Schafgans, B.-J. Kim, H.-T. Kim, Z. Cai, M. V. Holt, J. M. Maser, F. Keilmann, O. G. Shpyrko, and D. N. Basov, Phys. Rev. B **83**, 165108 (2011).

[26] M. K. Liu, M. Wagner, E. Abreu, S. Kittiwatanakul, A. McLeod, Z. Fei, M. Goldflam, S. Dai, M. M. Fogler, J. Lu, S. A. Wolf, R. D. Averitt, and D. N. Basov, Phys. Rev. Lett. **111**, 096602 (2013).

[27] M. K. Liu, M. Wagner, J. Zhang, A. Mcleod, S. Kittiwatanakul, Z. Fei, E. Abreu, M. Goldflam, A. J. Sternbach, S. Dai, K. G. West, J. Lu, S. A. Wolf, R. D. Averitt, and D. N. Basov, Appl. Phys. Lett. **104**, 121905 (2014).

[28] D. J. Hilton, R. P. Prasankumar, S. Fourmaux, A. Cavalleri, D. Brassard, M. A. El Khakani, J. C. Kieffer, A. J. Taylor, and R. D. Averitt, Phys. Rev. Lett. **99**, 226401 (2007).

[29] M. K. Liu, H. Y. Hwang, H. Tao, A. C. Strikwerda, K. Fan, G. R. Keiser, A. J. Sternbach, K. G. West, S. Kittiwatanakul, J. Lu, S. A. Wolf, F. G. Omenetto, X. Zhang, K. A. Nelson, and R. D. Averitt, Nature (London) **487**, 345 (2012).

[30] D. B. McWhan, T. M. Rice, and J. P. Remeika, Phys. Rev. Lett. **23**, 1384 (1969).

[31] D. B. McWhan, J. P. Remeika, T. M. Rice, W. F. Brinkman, J. P. Maita, and A. Menth, Phys. Rev. Lett. **27**, 941 (1971).

[32] D. B. McWhan, A. Menth, J. P. Remeika, W. F. Brinkman, and T. M. Rice, Phys. Rev. B **7**, 1920 (1973).

[33] M. M. Qazilbash, A. A. Schafgans, K. S. Burch, S. J. Yun, B. G. Chae, B. J. Kim, H. T. Kim, and D. N. Basov, Phys. Rev. B **77**, 115121 (2008).

[34] M. K. Stewart, D. Brownstead, S. Wang, K. G. West, J. G. Ramirez, M. M. Qazilbash, N. B. Perkins, I. K. Schuller, and D. N. Basov, Phys. Rev. B **85**, 205113 (2012).

[35] P. Hansmann, A. Toschi, G. Sangiovanni, T. Saha-Dasgupta, S. Lupi, M. Marsi, and K. Held, Phys. Status Solidi B **250**, 1251 (2013).

[36] D. B. McWhan and J. P. Remeika, Phys. Rev. B **2**, 3734 (1970).

[37] See Supplemental Material at http://link.aps.org/supplemental/10.1103/PhysRevB.92.085130 for details of the experimental setup, heating calculations, Avrami model fitting, and discussion of the scaling error and exponents.

[38] R. D. Averitt and A. J. Taylor, J. Phys.: Condens. Matter **14**, R1357 (2002).

[39] J.-G. Ramírez, A. Sharoni, Y. Dubi, M. E. Gómez, and I. K. Schuller, Phys. Rev. B **79**, 235110 (2009).

[40] M. I. Kaganov, I. M. Lifshitz, and L. V. Tanatarov, Sov. Phys. JETP **4**, 173 (1957).

[41] S. I. Anisimov, B. L. Kapeliovich, and T. L. Perel'man, Sov. Phys. JETP **66**, 375 (1974).

[42] P. B. Allen, Phys. Rev. Lett. **59**, 1460 (1987).

[43] H. V. Keer, D. L. Dickerson, H. Kuwamoto, H. L. C. Barros, and J. M. Honig, J. Solid State Chem. **19**, 95 (1976).

[44] J. H. Bechtel, J. Appl. Phys. **46**, 1585 (1975).

[45] J. Demsar, M. Zavrtanik, B. Podobnik, V. I. Dediu, and D. Mihailovic, J. Supercond. **10**, 455 (1997).

[46] H. Wen, L. Guo, E. Barnes, J. H. Lee, D. A. Walko, R. D. Schaller, J. A. Moyer, R. Misra, Y. Li, E. M. Dufresne, D. G. Schlom, V. Gopalan, and J. W. Freeland, Phys. Rev. B **88**, 165424 (2013).

[47] A. D. Caviglia, R. Scherwitzl, P. Popovich, W. Hu, H. Bromberger, R. Singla, M. Mitrano, M. C. Hoffmann, S. Kaiser, P. Zubko, S. Gariglio, J.-M. Triscone, M. Först, and A. Cavalleri, Phys. Rev. Lett. **108**, 136801 (2012).

[48] D. I. Khomskii, *Basic Aspects of the Quantum Theory of Solids: Order and Elementary Excitations* (Cambridge University Press, Cambridge, 2010).

[49] K. Binder, Rep. Prog. Phys. **50**, 783 (1987).

[50] P. Chaikin and T. Lubensky, *Principles of Condensed Matter Physics* (Cambridge University Press, Cambridge, 2000).

[51] S. Lupi, L. Baldassarre, B. Mansart, A. Perucchi, A. Barinov, P. Dudin, E. Papalazarou, F. Rodolakis, J.-P. Rueff, J.-P. Itié, S. Ravy, D. Nicoletti, P. Postorino, P. Hansmann, N. Parragh, A. Toschi, T. Saha-Dasgupta, O. K. Andersen, G. Sangiovanni, K. Held, and M. Marsi, Nat. Commun. **1**, 105 (2010).

[52] B. Mansart, A. Barinov, P. Dudin, L. Baldassarre, A. Perucchi, E. Papalazarou, P. Metcalf, S. Lupi, and M. Marsi, Appl. Phys. Lett. **100**, 014108 (2012).

[53] A. S. McLeod, E. Van Heumen, B. C. Chapler, M. D. Goldflam, M. K. Liu, L. Anderegg, S. Wang, J. G. Ramirez, S. Guenon, I. K. Schuller, and D. N. Basov, Bull. Am. Phys. Soc. J **49**, 11 (2014).

[54] H. S. Choi, J. S. Ahn, J. H. Jung, T. W. Noh, and D. H. Kim, Phys. Rev. B **54**, 4621 (1996).

[55] P. Papon, J. Leblond, and P. H. E. Meijer, *The Physics of Phase Transitions: Concepts and Applications*, Advanced Texts in Physics (Springer, Berlin, 2002), pp. 37–55.

[56] E. B. Shadrin and A. V. Il'inskii, Phys. Solid State **42**, 1126 (2000).

[57] R. Lopez, T. E. Haynes, L. A. Boatner, L. C. Feldman, and R. F. Haglund, Jr., Phys. Rev. B **65**, 224113 (2002).

[58] M. M. Seikh, C. Narayana, A. Sood, P. Murugavel, M. Kim, P. Metcalf, J. Honig, and C. Rao, Solid State Commun. **138**, 466 (2006).

[59] B. Rethfeld, K. Sokolowski-Tinten, D. von der Linde, and S. I. Anisimov, Phys. Rev. B **65**, 092103 (2002).

[60] J. G. Ramirez, T. Saerbeck, S. Wang, J. Trastoy, M. Malnou, J. Lesueur, J.-P. Crocombette, J. E. Villegas, and I. K. Schuller, Phys. Rev. B **91**, 205123 (2015).